Available online at www.sciencedirect.com
ScienceDirect
Journal of Bionic Engineering 12 (2015) 432–442

# Effects of Chordwise Flexibility on the Aerodynamic Performance of a 3D Flapping Wing

**Xin Cheng, Shilong Lan**

*Ministry-of-Education Key Laboratory of Fluid Mechanics*, *Beijing University of Aeronautics & Astronautics*, *Beijing*, *China*

**Abstract**

Previous studies on chordwise flexibility of flexible wings generally relied on simplified two-dimensional (2D) models. In the present study, we constructed a simplified three-dimensional (3D) model and identified the role of the chordwise flexibility in full flapping motion. This paper includes two parts, the first part discusses the aerodynamic effects of the chordwise flexibility in a typical hovering-flight case; the second part introduces a parametric study of four key parameters. The primary findings are as follows. Flexibility generally degrades the lift performance of the flexible wings. However, in two special cases, i.e. when stroke amplitude is low or pitch rotation is delayed, the flexible wings outperform their rigid counterparts in lift generation. Moreover, flexibility reduces the power consumption of the flexible wings. A wing with small flexibility generally achieves a marginally higher flapping efficiency than its rigid counterpart. Furthermore, reducing stroke amplitude can effectively improve the lift performance of the very flexible wings. Aerodynamic performances of the flexible wings are not as sensitive as the rigid wing to phase difference and mid-stroke angle of attack. The effects of *Re* are the same for the flexible and rigid wings.

**Keywords:** flapping wing, chordwise flexibility, aerodynamic performances, parametric study


doi: 10.1016/S1672-6529(14)60134-7

## 1 Introduction

The flapping flight of insects provides natural candidates for the development of biomimetic Micro Air Vehicles (MAVs). In recent years, many experimental and computational works have been done on flapping insect wings, and a sound understanding of the unsteady flight mechanisms has been achieved[1–7]. Previous studies generally rely on idealized rigid wing models, however, insect wings are intricate flexible structures that experience observational passive deformations during flight[8,9], which are more obvious around the stroke reversal[10]. The structural deformation during flapping may significantly change the flow behavior around the wing surface and consequently have an important effect on the aerodynamic performance of wings. What remains unknown is whether such structural deformation provides aerodynamic advantage or not, which should be specified to improve the design of MAVs.

Despite the diversity of species, insect wings are highly complex structures, consisting of venations supporting thin membranes without internal muscles that can actively change wing shape[11,12]. Therefore, the deformation during wing flapping mainly depends on the inertial, elastic and aerodynamic forces. The 3D Fluid-Structure Interaction (FSI) of flexible wing flight poses difficulty for numerical study, accurate and valid numerical computation methods for modeling such system are still scarce[13,14]. Combes and Daniel[15] reported that the inertial force due to acceleration of flapping wings and elastic force generated in wing deforming are obviously larger than the estimated aerodynamic forces, which suggests the possibility of decoupling the FSI problem and conducting numerical study with existing quantitative data on time-varying chordwise and spanwise twist of the realistic insect wings. Using the realistic deformation data measured by Walker *et al*.[10], Du and Sun[16] conducted a numerical study on the effects of wing deformation on aerodynamic forces of hoverflies. They found that, owing to the very high angle of attack (about 50°), the effects of wing deformation on aerodynamic forces were marginal. Zhao *et al*.[17] experimentally studied the effects of wing deformation,

**Corresponding author:** Xin Cheng
**E-mail:** x.cheng@buaa.edu.cn

employing a mechanical wing model consisting of rigid leading edge and a flexibility-alterable plastic plate. They proposed that flexible wings could generate forces slightly higher than the rigid model wing. Tanaka *et al*.[18] created an at-scale flexible polymer wing with tubular veins and corrugation profiles to mimick a hoverfly wing. Their results showed that, for the same flapping motions, a rigid wing can generate larger lift. However, the effects of wing flexibility on drag and efficiency were not investigated in their report.

Considering the structural complexity of insect wings, many numerical studies constructed simplified wing models for the coupled fluid-structure simulation. A simplified model is very meaningful for circumventing the difficulty of full elasticity aerodynamics, at the same time preserving the essential characteristics of the practical structure. The wing flexibility mainly consists of the spanwise twist and the chordwise chamber deformation[8–10]. Combes and Daniel[15] pointed out that the spanwise flexural stiffness of most insects was 1–2 orders of magnitude larger than chordwise flexible stiffness. Therefore, many investigations have been focused on studying the chordwise flexibility. Through a 2D two-component wing structure connected by a torsion spring modeling chordwise bending stiffness, Eldredge *et al*.[19] investigated the effect of chordwise wing flexibility for a wide variety of spring stiffnesses and kinematic parameters. They suggested that rigid wings consistently required more power consumption and a mildly flexible wing had consistently good performance over a wide range of phase differences between rotation and translation. Using a similar two-link model as described above (though covered by a set of aerodynamic surfaces for smoothness), Vanilla *et al*.[20] performed a 2D numerical simulation which focused on identifying the effects of torsion stiffness and Reynolds number. They characterized the wing flexibility by the ratio of stroke frequency to natural structural frequency and indicated that there existed a best performance which was achieved at a driven frequency 1/3 of the natural frequency. Yin and Luo[21] utilized a 2D elastic plate to model a chordwise flexible wing and studied the aerodynamic effect of wing inertia. They observed that the fluid force had aerodynamic advantages over the inertia force in dominating wing flexibility. Notice that the above studies[19–21] were all about 2D problems which lack some key features of a real 3D flapping wing, such as tip effects, strong vortex dissipation and spanwise-flow enhancement to the stability of Leading-Edge Vortex (LEV).

In this paper, we extended the 2D problem to a 3D case by utilizing a 3D two-component model to represent a chordwise flexible wing section. The leading portion of the wing is driven with prescribed flapping kinematics, whilst the aft portion responds passively to aerodynamic, elastic and inertial forces. Thus, the complex structural problem is simplified to a rigid-body dynamic problem with only one unknown parameter, i.e., the deflection angle ($\theta$) defined in section **2.2**. We derived the 3D structural dynamic equations and solved them together with the Navier-Stokes (N-S) equations by using a weakly coupled FSI scheme. The aim of this research is to investigate how the chordwise flexibility affects the aerodynamic performance of a flapping wing in 3D cases. Firstly, a typical case was considered in which typical values of wing kinematic parameters were used, and the effects the chordwise flexibility on lift and power consumption of flexible wings were analyzed in detail. Secondly, a parametric study was conducted to investigate the influences of three key kinematic parameters and Reynolds number ($Re$) on aerodynamic performances, which helped answer the question about whether or not the previous results of parametric study for rigid wings still apply to flexible wings. It should be kept in mind that the two-component model in present study is just a kind of simple and feasible configuration for the insect-sized MAVs, which may have some differences from the deformations of true insect wings in nature.

## 2 Materials and methods

### 2.1 Stroke kinematics

For simplicity, the wing used in present study is a rectangular flat plate of 3% thickness of the chord length of the wing ($c$) with round leading and trailing edges. The aspect ratio, i.e. the ratio of the wing length ($R$) to the chord length of the wing, is 3. The radius of the second moment of wing area, $r_2$, is $0.56R$; the mean flapping velocity at span location $r_2$ is used as reference velocity $U$, see below for the definition of $U$. The stroke kinematics are the same as those used previously in Sun and Tang[22] that originated from the experiments of Dickinson *et al*.[2]. The flapping motion of the wing consists of two parts: the translation or azimuthal rota-

tion around $Z$-axis, and the flip rotation or rotation around $y'$-axis (see Fig. 1a). Let $\phi$ denote the azimuthal angle and $\dot{\phi}$ the rotational velocity, which takes a constant value ($\dot{\phi}_0$) except at the start or near the end of a stroke. The time variation of $\dot{\phi}$ (see Fig. 1b) during a stroke reversal is given by

$$\dot{\phi}^+ = \dot{\phi}_0^+ \cos[\pi(\tau - \tau_t - \Delta\tau_t)/\Delta\tau_t], \quad \tau_t \le \tau \le \tau_t + \Delta\tau_t, \tag{1}$$

where the non-dimensional form $\dot{\phi}^+ = \dot{\phi}c/U$, $\dot{\phi}_0^+ = \dot{\phi}_0 c/U$, $\tau = tU/c$. The non-dimensional time duration of deceleration and acceleration around $Z$-axis is $\Delta\tau_t$ and the non-dimensional time when deceleration starts is $\tau_t$. The reference velocity is $U$, defined as $U = 2\Phi n r_2$, where $\Phi$ and $n$ are the stroke amplitude and frequency of the wing, respectively. Thus, the period of wingbeat cycle, $\tau_c$ ($=U/cn$), is related to $\Phi$ by $\tau_c = 2\Phi r_2/c$. In this time interval of $\Delta\tau_t$, $\dot{\phi}$ changes from $-\dot{\phi}_0$ to $+\dot{\phi}_0$ (around the next stroke reversal, $\dot{\phi}$ should change from $+\dot{\phi}_0$ to $-\dot{\phi}_0$, so the sign of the right-hand side of Eq. (1) should be reversed).

The angle of attack of the wing ($\alpha$) is also assumed constant ($\alpha_m$, the mid-stroke angle of attack) except at the start or near the end of a stroke. During stroke reversal, $\alpha$ changes with time and the angular velocity $\dot{\alpha}$ (see Fig. 1b) is given by

$$\dot{\alpha}^+ = 0.5\dot{\alpha}_0^+\{1 - \cos[2\pi(\tau - \tau_r)/\Delta\tau_r]\}, \quad \tau_r \le \tau \le \tau_r + \Delta\tau_r, \tag{2}$$

where the non-dimensional form $\dot{\alpha}^+ = \dot{\alpha}c/U$, $\dot{\alpha}_0^+$ is a constant. The time duration of wing rotation around $y'$-axis is $\Delta\tau_r$ and the time when flip rotation starts is $\tau_r$. In the time interval of $\Delta\tau_r$, the wing rotates from $\alpha = \alpha_m$ to $\alpha = 180^\circ - \alpha_m$ (around the next stroke reversal, the wing should rotate from $\alpha = 180^\circ - \alpha_m$ to $\alpha = \alpha_m$, and the sign of the right-hand side of Eq. (2) should be reversed). When $\tau_r$ is chosen such that the wing already flips over the vertical position by the end of a stroke, it is called advanced rotation mode; when $\tau_r$ is chosen such that the wing flips just in vertical position by the end of a stroke, it is called symmetrical rotation mode; when $\tau_r$ is chosen such that the wing has not reach the vertical position by the end of a stroke, it is called delayed rotation mode. For better understanding, phase difference ($\Psi$) is introduced, which indicates the phase lead of rotation relative to translation at the instant of stroke reversal. $\Psi > 0^\circ$, $\Psi = 0^\circ$ and $\Psi < 0^\circ$ respectively correspond to the advanced, symmetrical and delayed rotation modes.

In the flapping motion described above, $\Phi$, $\Psi$ and $\alpha_m$ are the three key kinematic parameters that need to be specified. The Reynolds number ($Re$), which appears in the non-dimensional N-S equations, is defined as $Re = cU/\upsilon$ (where $\upsilon$ is the kinematic viscosity of the air).

### 2.2 Wing dynamic equations and numerical algorithms

The 3D model used in this study is depicted in Fig. 2. The leading and aft portions of the wing are connected by a hinge with linear torsion spring. The kinematics of the leading (driven) portion is prescribed and the aft (passive) portion responds passively. The hinge is located at a distance $0.5c$ from the leading edge of the wing and the chordwise flexibility is modeled by the spring stiffness $K$ of the hinge (no damping coefficient is considered in this study). The angular deflection of the aft portion is measured by $\theta$ (Fig. 2), which together with azimuthal angle $\phi$ and attack angle $\alpha$, is used to determine the position of the two-component wing. The

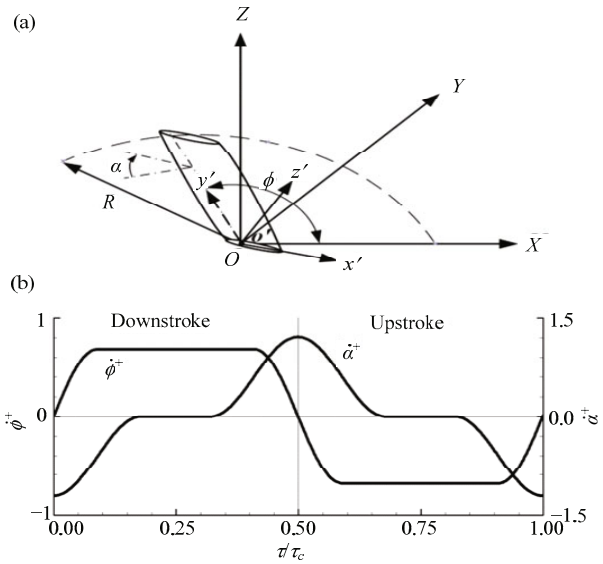


**Fig. 1** (a) Sketches of the reference frames and wing motion. $OXYZ$ is an inertial frame, the wing rotates about $Z$-axis and the azimuthal angle is denoted by $\phi$, the $XY$ plane is the stroke plane. $o'x'y'z'$ is a frame fixed on the wing, with the $x'$-axis along the wing chord line and the $y'$-axis located at one quarter of chord from leading edge along the wing span, acting like pitching axis in propeller, that is, the wing also rotates about $y'$-axis and geometrical angle of attack of the wing is denoted by $\alpha$, i.e. the angle between the chord line and stroke plane; $R$, wing length. (b) Non-dimensional angular velocity of pitching rotation $\dot{\alpha}^+$ and azimuthal rotation $\dot{\phi}^+$ in a typical case.

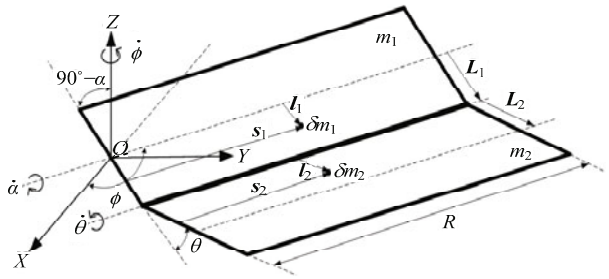


**Fig. 2** Model system consisting of two rigid plate sections connected by a hinge with torsion spring.

corresponding angular velocity vectors are $\dot{\boldsymbol{\theta}}$, $\dot{\boldsymbol{\phi}}$ and $\dot{\boldsymbol{\alpha}}$ (Fig. 2). The total mass of the leading portion is denoted by $m_1$ and the corresponding mass element is defined as $\delta m_1$. The vector from medial axis of the leading portion to the hinge axis is $\boldsymbol{L}_1$, and the vector from point $O$, origin of the inertial frame $OXYZ$, to the element mass $\delta m_1$ includes two components: $\boldsymbol{l}_1$ and $\boldsymbol{s}_1$ (Fig. 2). The total mass $m_2$, mass element $\delta m_2$ and distance vectors $\boldsymbol{L}_2$, $\boldsymbol{l}_2$ and $\boldsymbol{s}_2$ of the aft portion are defined in a similar way as described above.

The dynamic equation for the deflection angle $\theta$ of the aft portion can be derived with Lagrange's equation

$$\frac{\mathrm{d}}{\mathrm{d}t}\left(\frac{\partial L}{\partial \dot{\theta}}\right)-\frac{\partial L}{\partial \theta}=Q_\theta, \tag{3}$$

where $L=T-V$ (kinetic energy − potential energy) is the Lagrange function and $Q_\theta$ is the generalized force.

Firstly, we give the kinetic energy of the system

$$T=T_{m_1}+T_{m_2}=\iint_{2L_1R}\frac{1}{2}\delta m_1(\boldsymbol{v}_{\delta m_1})^2+\iint_{2L_2R}\frac{1}{2}\delta m_2(\boldsymbol{v}_{\delta m_2})^2, \tag{4}$$

where $\delta m_1=\dfrac{m_1\mathrm{d}l_1\mathrm{d}s_1}{2L_1R}$, $\delta m_2=\dfrac{m_2\mathrm{d}l_2\mathrm{d}s_2}{2L_2R}$, $\boldsymbol{v}_{\delta m_1}$ and $\boldsymbol{v}_{\delta m_2}$ are the corresponding velocity vectors and have the form

$$\boldsymbol{v}_{\delta m_1}=\dot{\boldsymbol{\phi}}\times(\boldsymbol{s}_1+\boldsymbol{l}_1)+\dot{\boldsymbol{\alpha}}\times\boldsymbol{l}_1, \tag{5}$$

$$\boldsymbol{v}_{\delta m_2}=\dot{\boldsymbol{\phi}}\times(\boldsymbol{s}_2+\boldsymbol{l}_1+\boldsymbol{l}_2)+\dot{\boldsymbol{\alpha}}\times(\boldsymbol{l}_1+\boldsymbol{l}_2)+\dot{\boldsymbol{\theta}}\times\boldsymbol{l}_2. \tag{6}$$

The potential energy of the system is given by

$$V=\frac{1}{2}K\theta^2, \tag{7}$$

The generalized force is given by

$$Q_\theta=[\delta W]_{\delta\theta}/\delta\theta=T_{\mathrm{fluid},\theta}\delta\theta/\delta\theta=T_{\mathrm{fluid},\theta}, \tag{8}$$

where $W$ stands for the virtual work and $T_{\mathrm{fluid},\theta}$ denotes the moment about the hinge axis exerted by the fluid on the aft portion of the wing, which is obtained from numerical calculation.

Substituting Eqs. (4) – (8) into Eq. (3), we obtain

$$\begin{aligned}\frac{4}{3}m_2L_2^2\ddot{\theta}=&-K\theta-\left(\frac{4}{3}m_2L_2^2+m_2L_1L_2\cos\theta\right)\ddot{\alpha}\\&-m_2L_1L_2\sin\theta\dot{\alpha}^2+\frac{1}{2}m_2L_2R\sin(\alpha-\theta)\ddot{\phi}\\&+\frac{2}{3}m_2L_2^2\sin(2\alpha-2\theta)\dot{\phi}^2\\&+m_2L_1L_2\cos\alpha\sin(\alpha-\theta)\dot{\phi}^2+T_{\mathrm{fluid},\theta}.\end{aligned} \tag{9}$$

Taking the chord length $c$, density of fluid $\rho_f$ and wingbeat frequency $n$ as the reference length, mass and time, respectively, we nondimensionalize Eq. (9) and have

$$\begin{aligned}\frac{4}{3}m_2^*L_2^{*2}\ddot{\theta}=&-K^*\theta-\left(\frac{4}{3}m_2^*L_2^{*2}+m_2^*L_1^*L_2^*\cos\theta\right)\ddot{\alpha}\\&-m_2^*L_1^*L_2^*\sin\theta\dot{\alpha}^2+\frac{1}{2}m_2^*L_2^*R^*\sin(\alpha-\theta)\ddot{\phi}\\&+\frac{2}{3}m_2^*L_2^{*2}\sin(2\alpha-2\theta)\dot{\phi}^2\\&+m_2^*L_1^*L_2^*\cos\alpha\sin(\alpha-\theta)\dot{\phi}^2+T_{\mathrm{fluid},\theta}^*,\end{aligned} \tag{10}$$

where $(\cdot)^*$ indicates the non-dimensional variables. In this paper, $m_2^*=0.96$, $L_1^*=L_2^*=0.25$ and $R^*=3$ are held constant. The non-dimensional spring stiffness, $K^*=K/(\rho_f n^2c^5)$, is varied between the values 5, 25 and 100, corresponding to flexible wings with large, medium and small flexibilities, respectively. An equivalent rigid wing is also considered for comparison. Eq. (10) is then integrated in time using a second-order predictor-corrector algorithm.

### 2.3 Flow equations and evaluation of the aerodynamic forces and mechanical power

The flow equations, numerical method and boundary conditions used in this paper were the same as those used by Sun *et al*. in previous studies[6,22,23]. The computational grid had dimensions 66×73×70 in the normal direction, around the wing section and in the spanwise direction, respectively. The normal grid spacing at the wall was $0.002c$ ($c$ is the chord length of wing). The outer boundary was set at 20 chord lengths from the wing and in the spanwise direction, the boundary was set seven chord lengths from wing root and wing tip. The non-dimensional time step was 0.02. The mesh size and

the time step were chosen according to the results of the grid-independent test and time accuracy test, which were not shown here for brevity. Portions of a wing grid with 30˚ chordwise deformation are shown in Fig. 3. Based on our results of the flow structures, such as vortex identified by $Q$-criterion, we found that the flow becomes nearly periodic after the first two cycles, since only very small difference could be discriminated in the following several cycles. Additionally, the variation of the deflection angle or the force history also shows periodicity after the first two cycles, which is consistent with the above vortex evolution.

After the N-S equations are numerically solved, the fluid velocity components and pressure at discretized grid points for each time step are available. The aerodynamic forces (lift, $L$; drag, $D$) and torques acting on the wing are calculated from the pressure and the viscous stress on the wing surface. The inertial torques due to the acceleration of the wing-mass are calculated analytically. The total mechanical power, $P$, is the combination of the power required to overcome the aerodynamic and inertial torques. The force and power coefficients (denoted as $C_L$, $C_D$ and $C_p$) are defined as follows: $C_L = L/0.5\rho U^2 S$ $C_D = D/0.5\rho U^2 S$ and $C_P = P/0.5\rho U^3 S$, where $\rho$ is the fluid density, $S$ the wing area, $U$ the mean flapping velocity and $c$ is the chord length. The wingbeat-cycle means of $C_L$, $C_P$ and $C_L/C_P$ are donated as $\overline{C}_L$, $\overline{C}_P$ and $\overline{C}_L / \overline{C}_P$ (regarded as the flapping efficiency), respectively. The formulae of the aerodynamic and inertial torques and the mechanical power were deduced in detail in Sun and Tang[22].

## 3 Results and discussion

### 3.1 A typical case

In the typical case, typical values of wing kinematic parameters were used ($Re$ = 200, $\Phi$ = 150˚, $\Psi$ = 0˚ and $\alpha_m$=35˚). Three flexible wings with various non-dimensional torsion stiffnesses were considered ($K^*$ = 5, 25 and 100). The larger the value of $K^*$, the smaller the chordwise flexibility is. Further, their aerodynamic performances were compared with an equivalent rigid wing.

The computed mean lift ($\overline{C}_L$), mean power ($\overline{C}_P$) and mean lift per unit power ($\overline{C}_L / \overline{C}_P$), averaged over one wingbeat cycle, are given in Table 1. From Table 1, compared with the flexible wings, the rigid wing generates the largest $\overline{C}_L$, but at the same time requires the maximum $\overline{C}_P$ to enable its flapping motion. In addition, the $\overline{C}_L$ and $\overline{C}_P$ of flexible wings decrease as flexibility increases, implying that the flexibility might have a negative effect on generating lift but a positive effect on reducing power consumption. The variation of $\overline{C}_L / \overline{C}_P$ arouses our high attention that the wing with small flexibility ($K^*$ = 100) achieves the highest efficiency (4.1% larger than that of the rigid wing). A possible explanation for this is that, in small flexibility cases, the positive effect of less power consumption outperforms the negative effect of lower lift generation. Higher efficiency leads to longer endurance for MAVs, which makes more sense in the case of the bottleneck our battery technology encounters today. How the lift performance of flexible wings is deteriorated and power consumption is reduced will be discussed below.

We first examine the time histories of $C_L$ and $C_D$ of the large flexible wing ($K^*$ = 5) and the rigid wing (Figs. 4a and 4b), together with that of $\theta$ of the $K^*$ = 5 wing (Fig. 4c). As seen in Fig. 4a, the large chordwise deformation markedly reduces $C_L$ as well as $C_D$ of the $K^*$ = 5 wing during the whole wingbeat cycle. Furthermore, the non-dimensional lift distributions along the wing length

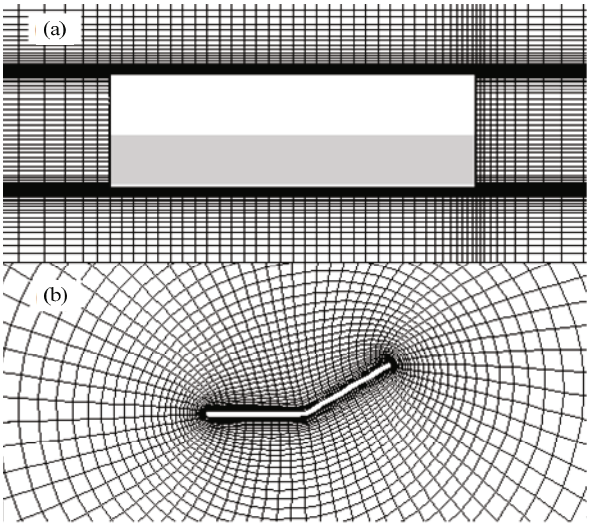


**Fig. 3** Portions of a wing grid with 30˚ chordwise deformation. (a) In the wing planform plane; (b) in the cross-sectional plane.

**Table 1** Computed mean lift, power and lift per unit power in the typical case (a number in the parenthesis represents the difference of mean lift or mean power or mean lift per unit power between each flexible wing and the rigid wing)

| $K^*$ | $\overline{C}_L$ | $\overline{C}_P$ | $\overline{C}_L / \overline{C}_P$ |
|---|---|---|---|
| +∞ | 1.40 | 2.20 | 0.636 |
| 100 | 1.33(−6.6%) | 2.01(−8.6%) | 0.662(4.1%) |
| 25 | 1.01(−27.9%) | 1.64(−25.5%) | 0.616(−3.1%) |
| 5 | 0.79(−43.6%) | 1.40(−36.4%) | 0.564(−11.3%) |

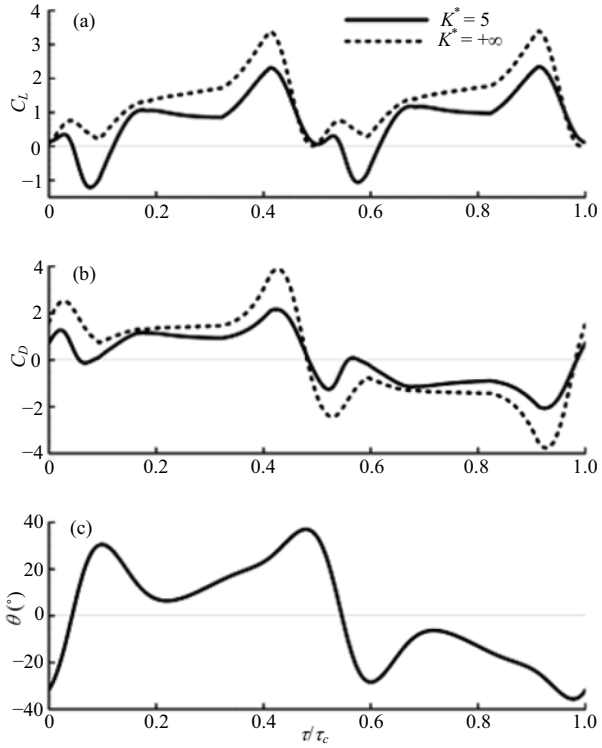


**Fig. 4** Time courses of lift coefficient (a) and drag coefficient (b) for the large flexible wing and the rigid wing in one cycle; time course of deflection angle (c) for the large flexible wing in one cycle. $Re = 200$, $\Phi = 150°$, $\Psi = 0°$ and $\alpha_m = 35°$.

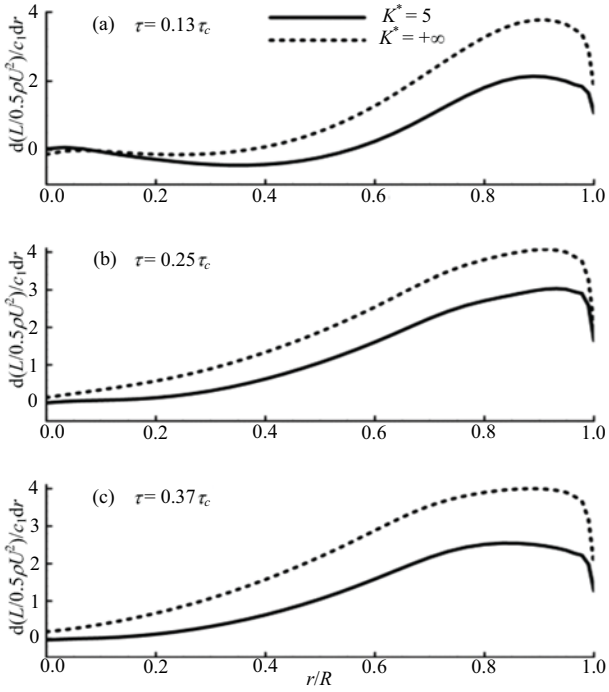


**Fig. 5** Non-dimensional lift distribution along wing length at early downstroke (a), mid-downstroke (b) and late downstroke (c) for the large flexible wing and the rigid wing.

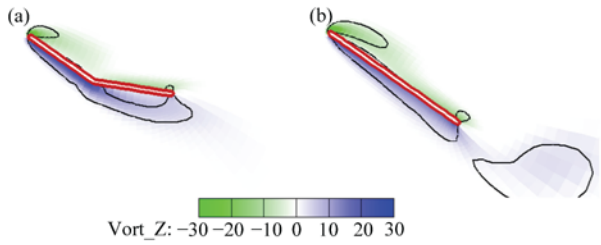


**Fig. 6** Spanwise vorticity contours at early downstroke ($\tau = 0.13\,\tau_c$) at $r_2$ span for the large flexible wing (a) and the rigid wing (b). The solid line is a single contour of the $Q$ criterion used in Fig. 7.

are shown in Fig. 5, which illustrates the spanwise lift distributions of the wing with $K^* = 5$ and the rigid wing at three instances during the downstroke. Fig. 5 shows that the influence of chordwise deflection on lift distribution of the wing with $K^* = 5$ varies uniformly along the span, possibly due to the uniform application of the chordwise hinge. As $C_L$ is closely related to growth rate of circulation of the LEV, it is reasonable to propose that the LEV strength of the wing with $K^* = 5$ also decreases uniformly down the span.

To investigate this further, the change in flow structures was assessed. Fig. 6 illustrates the spanwise vorticity at early downstroke ($\tau = 0.13\,\tau_c$) for the wing with $K^* = 5$ and the rigid wing. As seen in Fig. 6, the LEV structure of wing with $K^* = 5$ is smaller than that of the rigid wing, which is consistent with the lift coefficient difference shown in Fig. 4a. Moreover, at this point, the Trailing-Edge Vortex (TEV) of the rigid wing has already been shed from the wing, whilst the TEV of the wing with $K^* = 5$ has not been formed yet. The significant difference in TEV structures between the two wings can also be seen in Fig. 7, which illustrates the 3D change in vortex structures at three instances during early downstroke. For the rigid wing (right column in Fig. 7), in early downstroke, pitch rotation, together with translational acceleration, creates a vortex ring comprising a LEV, tip vortex (TV) and TEV. As the wing's motion continues, the TEV is shed from the wing while the LEV is still attached to the upper surface of wing, resulting in a large time rate of change of fluid impulse which is responsible for the generation of large aerodynamic forces[24]. For the wing with $K^* = 5$ (left column in Fig. 7), in early downstroke, the leading portion of the wing pitches down and accelerates forward, but the aft portion is negatively cambered, under the combined

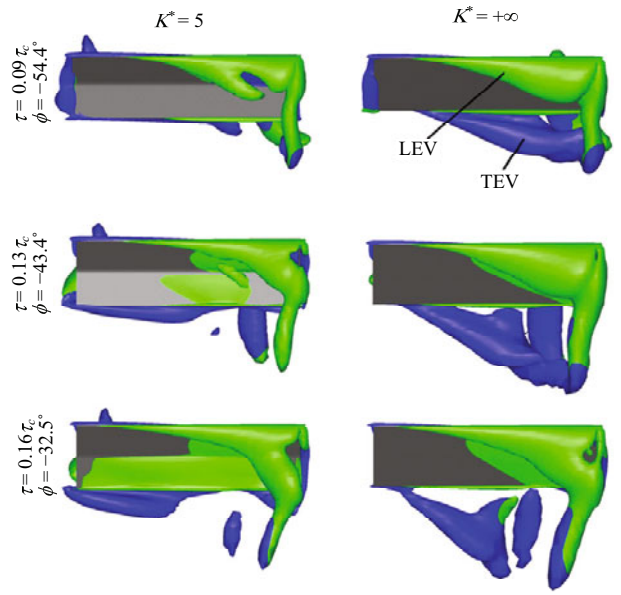


**Fig. 7** Iso-$Q$ ($Q$ = 5) surface plots of flow structures during the early downstroke ($\tau = 0.09\,\tau_c$ –$0.16\,\tau_c$) for wing with $K^*$ = 5 (left) and wing with $K^*$ = +∞ (right). Pictures are taken normal to the stroke plane of the wing. Vortex structures are shaded by spanwise vorticity to indicate direction: green is negative and blue is positive.

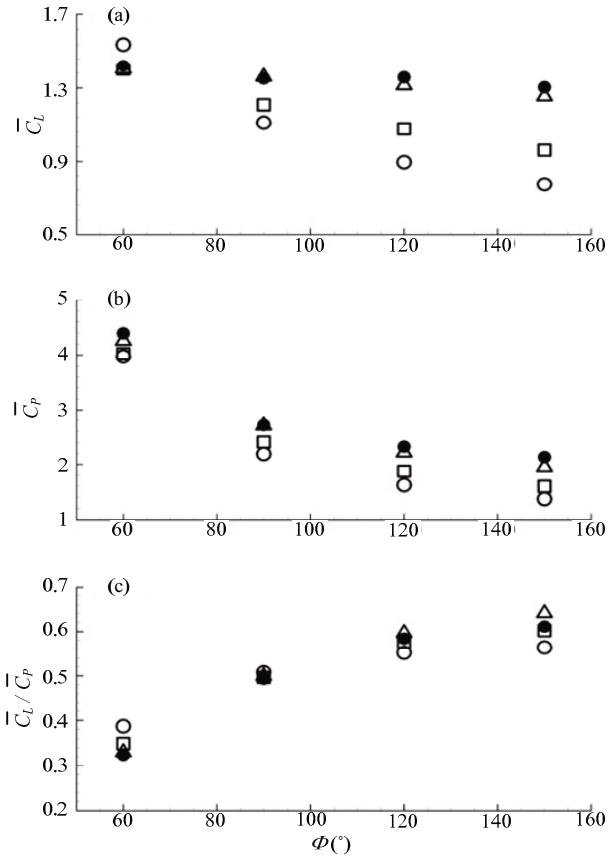


**Fig. 8** The effects of stroke amplitude on mean lift coefficient (a), mean power coefficient (b) and mean lift per unit power (c) for wings with various spring stiffnesses. ●, $K^*$=+∞; Δ, $K^*$=100; □, $K^*$=25; ○, $K^*$=5. $Re$=200, $\Psi$=0° and $\alpha_m$ = 35°.

action of elastic, inertial and aerodynamic torques. The large negative camber of the wing greatly suppresses the formation of TEV and thereby reduces the strength of LEV. Hence, during the subsequent flapping motion of the wing, smaller time rate of change of fluid impulse is experienced by the wing and therefore smaller lift is obtained. Furthermore, owing to the negative camber, flexible wings present smaller windward areas to the flow and experience smaller aerodynamic drags (Fig. 4b). Smaller drag results in less power consumption for the flexible wings.

### 3.2 The effects of stroke amplitude, phase difference, mid-stroke angle of attack and *Re*

Several previous studies[19–21] have discussed the effects of *Re*, wing inertia, stroke amplitude, phase difference, *etc*. on the aerodynamic performance of flexible wings in 2D cases, but their results are certainly inadequate as surrogates for 3D flapping wings. In this section, we conduct a parametric study on the effects of stroke amplitude ($\Phi$), phase difference ($\Psi$), mid-stroke angle of attack ($\alpha_m$) and Reynolds number ($Re$) (when analyzing the effects of a certain parameter, the other three parameters are kept the same as in the typical case). Results are reported for the three flexible wings with various non-dimensional spring stiffnesses and compared with the equivalent rigid wing. Based on the previous observational data and numerical studies of insects[1,2,6,25], $\Phi$ considered in this paper ranges from 60° to 150°, $\Psi$ from −45° to 45°, $\alpha_m$ from 25° to 60° and $Re$ from 50 to 2000. Performance is evaluated by comparing the mean lift ($\bar{C}_L$), power requirement ($\bar{C}_P$) and lift per unit power ($\bar{C}_L / \bar{C}_P$).

#### 3.2.1 The effects of stroke amplitude

The variation trends of $\bar{C}_L$, $\bar{C}_P$ and $\bar{C}_L / \bar{C}_P$ of the four wings with $\Phi$ are shown in Fig. 8. The lift of the rigid and stiffest flexible wings keeps nearly constant value, while the lift of the two most flexible wings drops with increasing $\Phi$ (Fig. 8a). These results are similar to the analysis of Eldredge *et al.*[19]. Moreover, the lift performances of the $K^*$ = 5 wing and the $K^*$ = 25 wing are markedly improved in small $\Phi$ cases (Fig. 8a). It is noteworthy that, in the case of $\Phi$ = 60°, chordwise flexibility seems to bring benefits for the $K^*$ = 5 wing to generate a $\bar{C}_L$ 8% larger than that of the rigid wing.

Notice that the dimensionless period of wingbeat cycle $\tau_c$ is related to $\Phi$ by $\tau_c = 2\Phi r_2/c$ and the dimensionless flip duration $\Delta\tau_r = 0.36\tau_c$ is fixed in this study. Thus, $\Delta\tau_r$ is proportional to $\Phi$ and the dimensionless angular velocity of pitch rotation $\dot{\alpha}^+$ increases as $\Phi$ decreases (Fig. 9a). In the $\Phi$ = 60° case, at the beginning of a stroke, the rotational velocity of the leading portion precedes the deflecting velocity of the aft portion, resulting in a positive camber for the $K^*$ = 5 wing (Fig. 9b and Fig. 10). The detrimental effect of negative camber disappears and a better lift performance is achieved by the $K^*$ = 5 wing in early downstroke and upstroke (Fig. 9c).

### 3.2.2 The effects of phase difference

Fig. 11 illustrates the variation trends of $\overline{C}_L$, $\overline{C}_P$ and $\overline{C}_L / \overline{C}_P$ of the four wings with $\Psi$. The 2D study of Eldredge *et al*.[19] suggested that there was a rapid fall in the lift of the rigid wing as $\Psi$ was increased. However, our results show that the lift of the rigid wing increases rapidly with $\Psi$ (Fig. 11a). The 2D result does not persist in full flapping. An explanation for the variation of lift of the rigid wing with respect to phase difference was given by previous studies[2,6] and will not be repeated here. For the flexible wings, the effects of varying $\Psi$ on $\overline{C}_L$ and $\overline{C}_P$ are not as obvious as for the rigid wing (Figs. 11a and 11b). It is interesting to note that, in the case of $\Psi$ = −45°, the $K^*$ = 100 wing generates a $\overline{C}_L$ with 41% larger than that of the rigid wing. This phenomenon is highlighted and is further studied as shown below. In the $\Psi$ = −45° case, the rotation of the wing is greatly delayed with respect to stroke reversal, i.e., the majority of the rotation is done in the beginning of the next stroke (Fig. 12a). Large chordwise deformation is experienced by the $K^*$ = 100 wing during this period (Fig. 12b), resulting in significant lift enhancement compared with the rigid wing (Fig. 12c). This behavior can be better understood by comparing the sectional vorticity contour plots and vortex structures between the two wings. Fig. 13 illustrates the change in vortex structures and their corresponding spanwise vorticities at $r_2$ span at three instants during early downstroke for the $K^*$ = 100 wing (left) and the rigid wing (right). At $\tau = 0.09\tau_c$, the rigid wing flips just in the vertical position and a strong LEV is formed at the leading edge of the wing. As it continues to rotate, due to the rapid pitching-down rotation and the fast translational acceleration, the LEV is shed and a new LEV is under development. Thus, small or even negative lift is generated for the rigid wing during this period. The $K^*$ = 100 wing, however, experiences large deformation during the rapid rotation and acceleration at the start of stroke ($\theta$ reaches the maximum value 56.2° at $\tau = 0.07\tau_c$). The elastic potential energy stored by the hinge spring drives the aft portion to rotate clockwise and develop a strong TEV near the trailing edge (left column in Fig. 13). Moreover, the clockwise rotation of the aft

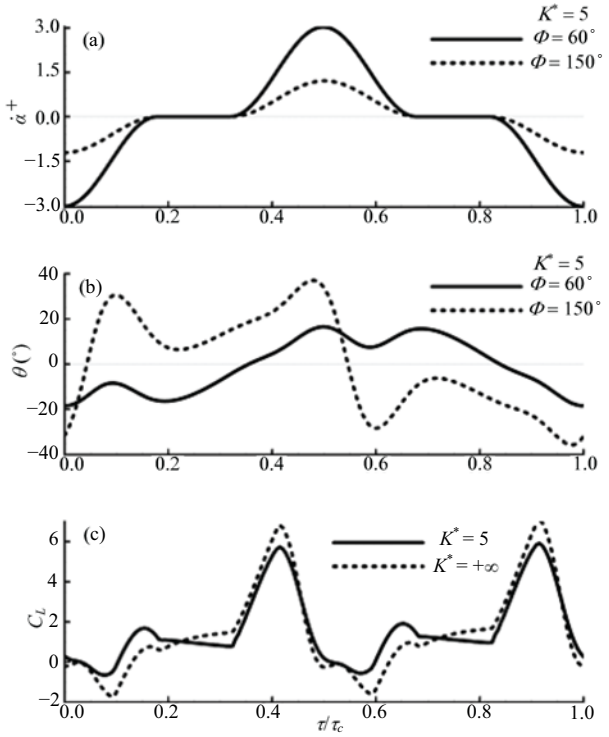


**Fig. 9** Time courses of non-dimensional angular velocity of pitching rotation $\dot{\alpha}^+$ (a) and deflection angle $\theta$ (b) in one cycle for the large flexible wing in $\Phi$ = 60° and $\Phi$ = 150° cases. Time courses of lift coefficient for the large flexible wing and the rigid wing in one cycle in the $\Phi$ = 60° case (c). $Re$ = 200, $\Psi$ = 0° and $\alpha_m$ = 35°.

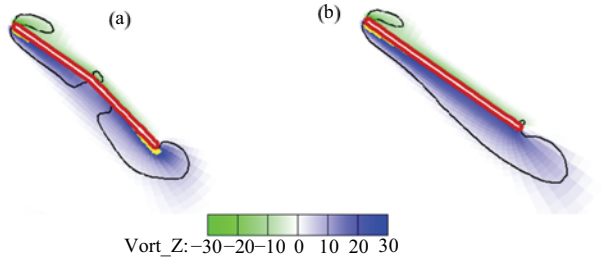


**Fig. 10** Spanwise vorticity contours at early downstroke ($\tau$ = 0.13$\tau_c$) at $r_2$ span in the $\Phi$ = 60° case for the large flexible wing (a) and the rigid wing (b). The solid line is a single contour of the $Q$ criterion ($Q$ = 5).

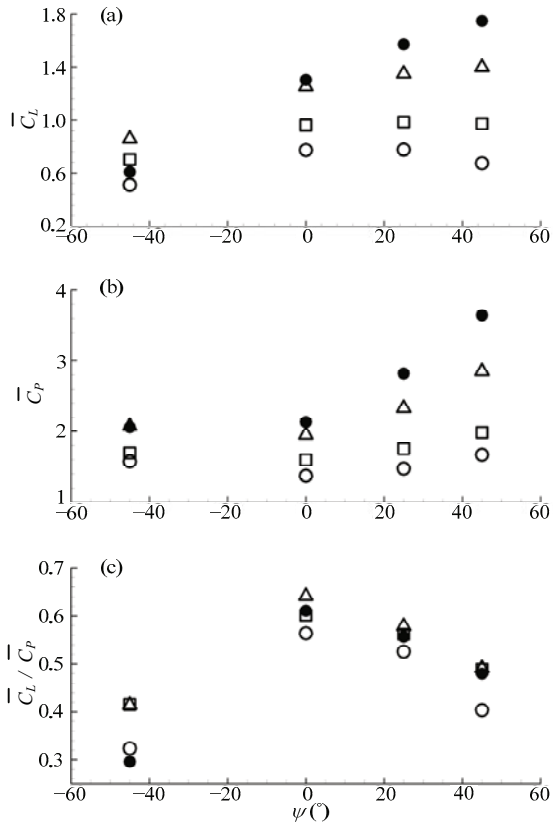


**Fig. 11** The effects of phase difference on mean lift coefficient (a), mean power coefficient (b) and mean lift per unit power (c) for wings with various spring stiffnesses. ●, $K^*$=+∞; Δ, $K^*$=100; □, $K^*$=25; ○, $K^*$=5. $Re$=200, $\Phi$=150° and $\alpha_m$ = 35°.

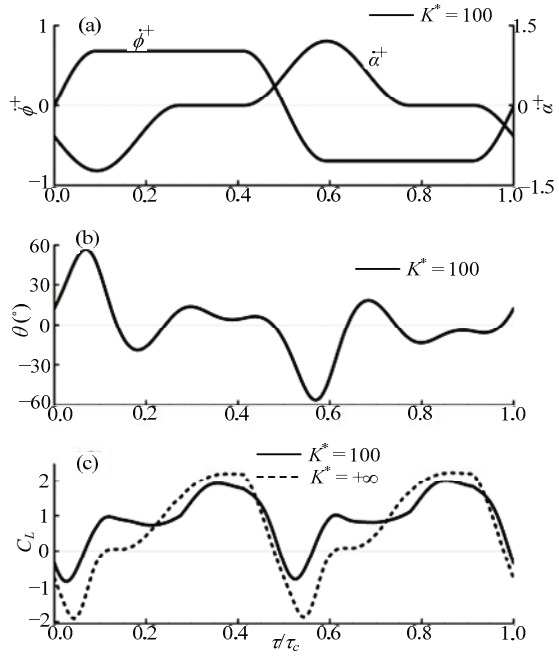


**Fig. 12** Time courses of non-dimensional angular velocity of pitching rotation $\dot{\alpha}^+$ and azimuthal rotation $\dot{\phi}^+$ (a), deflection angle $\theta$ (b) and lift coefficient (c) in one cycle for the wing with small chordwise flexibility and the rigid wing in $\Psi$ = −45° case. $Re$ = 200, $\Phi$ = 150° and $\alpha_m$ = 35°.

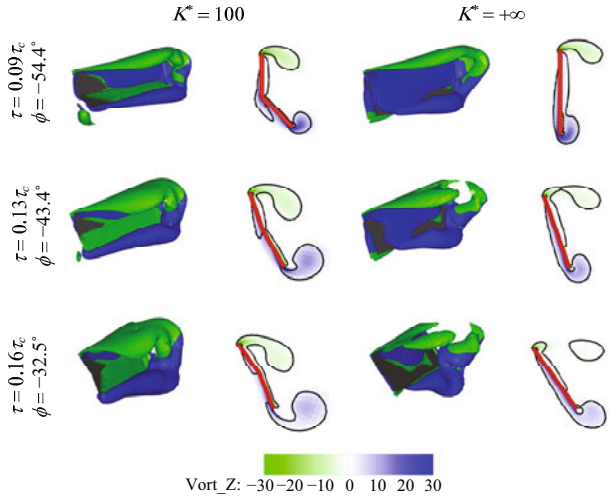


**Fig. 13** Iso-$Q$ ($Q$ = 5) surface plots of flow structures and their corresponding spanwise vorticities at $r_2$ span during the early downstroke ($\tau$ = 0.09 $\tau_c$ − 0.16 $\tau_c$) for $K^*$=100 wing (left) and $K^*$=+∞ wing (right). Pictures of vortex structures are taken from a stationary view. Vortex structures are shaded by spanwise vorticity to indicate direction: green is negative and blue is positive. The solid line in spanwise vorticity contours is a single contour of the $Q$ criterion ($Q$ = 5).

portion creates a downward suction which stabilizes the LEV. The attached LEV, together with the strong TEV, generates a large time rate of change of fluid impulse and hence large lift.

### 3.2.3 The effects of mid-stroke angle of attack

The effects of $\alpha_m$ on $\bar{C}_L$, $\bar{C}_P$ and $\bar{C}_L / \bar{C}_P$ for the four wings are displayed in Fig. 14. It is common knowledge for rigid wings that, the lift and power consumption will both increase as the $\alpha_m$ increases within certain limits. However, for the flexible wings, the deflection of the aft portion becomes larger with the increase of $\alpha_m$ and larger deformation leads to worse lift performance and less power consumption (Figs. 14a and 14b). As seen in Fig. 14c, almost all wings achieve the highest efficiency at a moderate $\alpha_m$, which indicates that, although increasing $\alpha_m$ is an optional choice for lift-enhancement, there is a penalty of more power consumption.

### 3.2.4 The effects of *Re* number

As seen in Fig. 15, the variation trends of $\bar{C}_L$, $\bar{C}_P$ and $\bar{C}_L / \bar{C}_P$ with $Re$ are the same for the three flexible wings and the rigid wing, which implies that the previous explanations[26] for the effects of $Re$ in rigid wing cases can also apply to the flexible wings considered

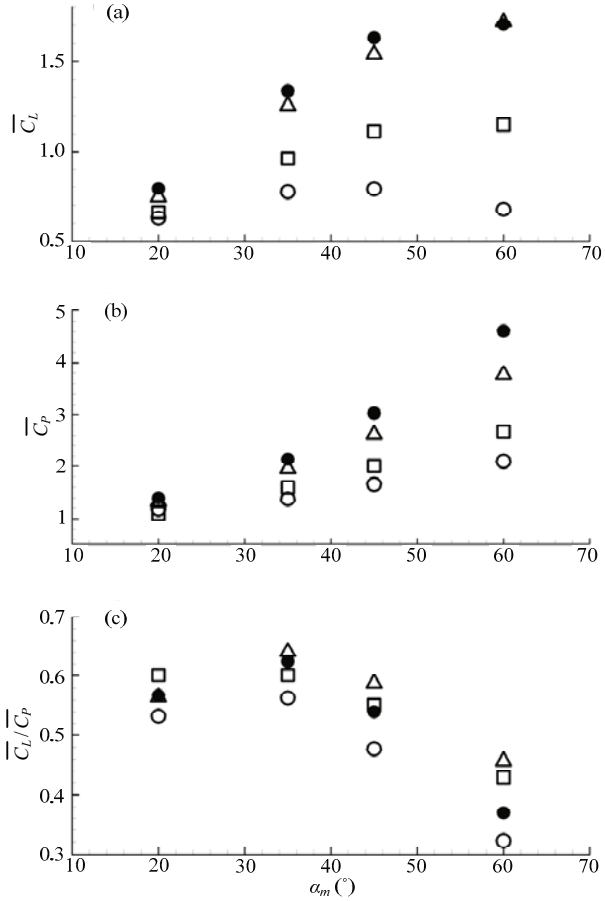


**Fig. 14** The effects of mid-stroke angle of attack on mean lift coefficient (a), mean power coefficient (b) and mean lift per unit power (c) for wings with various spring stiffnesses. ●, $K^*=+\infty$; Δ, $K^*=100$; □, $K^*=25$; ○, $K^*=5$. $Re=200$, $\Phi=150^\circ$ and $\Psi=0^\circ$.

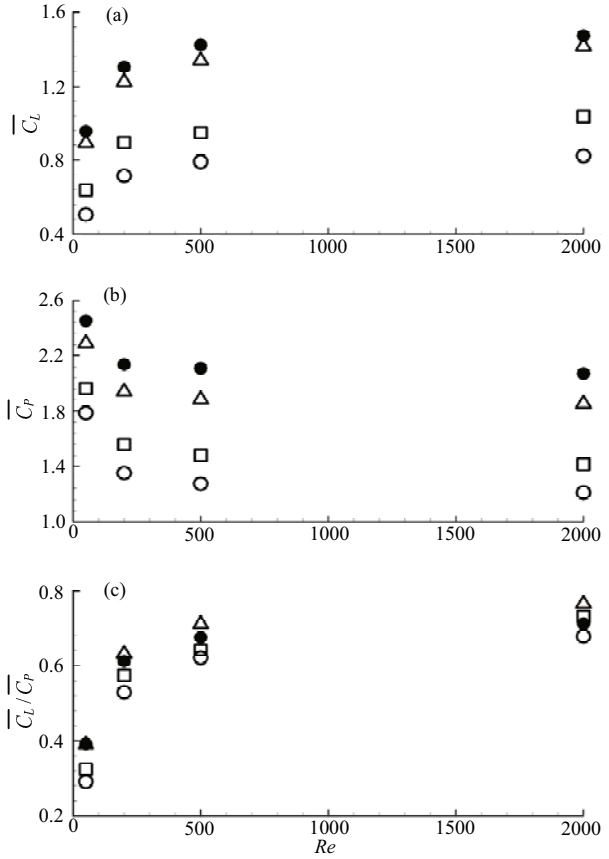


**Fig. 15** The effects of Reynolds number on mean lift coefficient (a), mean power coefficient (b) and mean lift per unit power (c) for wings with various spring stiffnesses. ●, $K^*=+\infty$; Δ, $K^*=100$; □, $K^*=25$; ○, $K^*=5$. $\Phi=150^\circ$, $\Psi=0^\circ$ and $\alpha_m=35^\circ$.

in this paper. Our results agree with the analysis of Vanella *et al*.[20], in which the variations of aerodynamic quantities with respect to flexibility show similar characteristics for all *Re* considered. Owing to the low *Re* and therefore high viscous diffusion, the LEV in $Re=50$ case is highly weak and diffused compared with that in higher *Re* cases, resulting in small $\overline{C}_L$ and large $\overline{C}_P$ (Figs. 15a and 15b).

## 4 Conclusion

In this paper, we focus on the 3D effect of the chordwise flexibility. Firstly, a typical case is considered. The results demonstrate that the negative camber due to deflection has a negative effect in generating lift but a positive effect in reducing power consumption. Moreover, the wing with small chordwise flexibility achieves a higher efficiency than the rigid wing. We suggest that there exists an optimal $K^*$ that can achieve the highest flapping efficiency. However, it is noteworthy that the optimal $K^*$ varies with different cases. Secondly, a parametric study is conducted. The results are as follows. Significant difference is observed between the flexible wings and their rigid counterparts in the effects of stroke amplitude, phase difference and mid-stroke angle of attack. Reducing stroke amplitude can improve the lift performance of the flexible wings while changing phase difference and mid-stroke angle of attack are not efficient methods to change force behaviors for flexible wings. Furthermore, the effects of *Re* are the same for the flexible wings and their rigid counterparts.

In the present study, the chordwise flexibility is varied by only changing the torsion stiffness of the hinge. More work is still needed to quantify the dependence of chordwise flexibility on wing structure properties (e.g. natural structural frequency, wing-fluid density ratio). This issue will be explored in future work.

## References


[1] Ellington C P, van den Berg C, Willmott A P, Thomas A L R. Leading-edge vortices in insect flight. *Nature*, 1996, **384**, 626–630.

[2] Dickinson M H, Lehman F O, Sane S P. Wing rotation and the aerodynamic basis of insect flight. *Science*, 1999, **284**, 1954–1960.

[3] Sane S P, Dickinson M H. The control of flight force by a flapping wing: Lift and drag production. *Journal of Experimental Biology*, 2001, **204**, 2607–2626.

[4] Usherwood J R, Ellington C P. The aerodynamics of revolving wings. I. Model hawkmoth wings. *Journal of Experimental Biology*, 2002, **205**, 1547–1564.

[5] Usherwood J R, Ellington C P. The aerodynamics of revolving wings. II. Propeller force coefficients from mayfly to quail. *Journal of Experimental Biology*, 2002, **205**, 1565–1576.

[6] Sun M, Tang J. Unsteady aerodynamic force generation by a model fruit fly wing in flapping motion. *Journal of Experimental Biology*, 2002, **205**, 55–70.

[7] Wang Z J, Birch J M, Dickinson M H. Unsteady forces and flows in flow Reynolds number hovering flight: Two-dimensional computational vs robotic wing experiments. *Journal of Experimental Biology*, 2004, **207**, 269–283.

[8] Ellington C P. The aerodynamics of hovering insect flight. III. Kinematics. *Philosophical Transactions of the Royal Society of London B*: *Biological Sciences*, 1984, **305**, 41–78.

[9] Ennos A R. The kinematics and aerodynamics of the free flight of some Diptera. *Journal of Experimental Biology*, 1989, **142**, 49–85.

[10] Walker S M, Thomas A L R, Taylor G K. Deformable wing kinematics in free-flying hoverflies. *Journal of the Royal Society Interface*, 2009, **7**, 131–142.

[11] Dudley R. *The Biomechanics of Insect Flight*: *Form*, *Function*, *Evolution*, Princeton University Press, 2000.

[12] Wootton R J, Herbert R C, Young P G, Evans K E. Approaches to the structural modelling of insect wings. *Philosophical Transactions of the Royal Society of London B*: *Biological Sciences*, 2003, **358**, 1577–1587.

[13] Nakata T, Liu H. Aerodynamic performance of a hovering hawkmoth with flexible wings: A computational approach. *Proceedings of the Royal Society B*: *Biological Sciences*, 2012, **279**, 722–731.

[14] Tian F B, Dai H, Luo H, Doyle J F, Rousseau B. Fluid–structure interaction involving large deformations: 3D simulations and applications to biological systems. *Journal of Computational Physics*, 2014, **258**, 451–469.

[15] Combes S A, Daniel T L. Flexural stiffness in insect wings: Effects of wing venation and stiffness distribution on passive bending. *American Entomologist*, 2005, **51**, 42–44.

[16] Du G, Sun M. Effects of wing deformation on aerodynamic forces in hovering hoverflies. *Journal of Experimental Biology*, 2010, **213**, 2273–2283.

[17] Zhao L, Huang Q, Deng X, Sane S P. Aerodynamic effects of flexibility in flapping wings. *Journal of the Royal Society Interface*, 2010, **7**, 485–497.

[18] Tanaka H, Whitney J P, Wood R J. Effect of flexural and torsional wing flexibility on lift generation in hoverfly flight. *Integrative and Comparative Biology*, 2011, **51**, 142–150.

[19] Eldredge J D, Toomey J, Medina A. On the roles of chord-wise flexibility in a flapping wing with hovering kinematics. *Journal of Fluid Mechanics*, 2010, **659**, 94–115.

[20] Vanella M, Fitzgerald T, Preidikman S, Balaras E, Balachandran B. Influence of flexibility on the aerodynamic performance of a hovering wing. *Journal of Experimental Biology*, 2009, **212**, 95–105.

[21] Yin B, Luo H. Effect of wing inertia on hovering performance of flexible flapping wings. *Physics of Fluids*, 2010, **22**, 111902.

[22] Sun M, Tang J. Lift and power requirements of hovering flight in Drosophila virilis. *Journal of Experimental Biology*, 2002, **205**, 2413–2427.

[23] Sun M, Xiong Y. Dynamic flight stability of a hovering bumblebee. *Journal of Experimental Biology*, 2005, **208**, 447–459.

[24] Lan S L, Sun M. Aerodynamic properties of a wing performing unsteady rotational motions at low Reynolds number. *Acta mechanica*, 2001, **149**, 135–147.

[25] Fry S N, Sayaman R, Dickinson M H. The aerodynamics of free-flight maneuvers in Drosophila. *Science*, 2003, **300**, 495–498.

[26] Wu J H, Sun M. Unsteady aerodynamic forces of a flapping wing. *Journal of Experimental Biology*, 2004, **207**, 1137–1150.